Journal of Cleaner Production 414 (2023) 137701

Contents lists available at ScienceDirect

Journal of Cleaner Production

journal homepage: www.elsevier.com/locate/jclepro

# Understanding stability, oligomerization and deactivation during catalytic lignin hydrodeoxygenation by mechanistic reaction micro-kinetics linked with 3D catalyst particle nanotomography

Tina Ročnik Kozmelj [a,b], Matej Žula [a,b], Janvit Teržan [a], Blaž Likozar [a], Uroš Maver [c,d], Laura Činč Ćurić [c], Edita Jasiukaitytė-Grojzdek [a,**], Miha Grilc [a,b,*]

[a] Department of Catalysis and Chemical Reaction Engineering, National Institute of Chemistry, Hajdrihova 19, 1000, Ljubljana, Slovenia
[b] University of Nova Gorica, Vipavska 13, 5000, Nova Gorica, Slovenia
[c] University of Maribor, Faculty of Medicine, Institute of Biomedical Sciences, Taborska ulica 8, 2000, Maribor, Slovenia
[d] University of Maribor, Faculty of Medicine, Department of Pharmacology, Taborska ulica 8, 2000, Maribor, Slovenia

ARTICLE INFO

Handling Editor: Cecilia Maria Villas Bôas de Almeida

*Keywords:*
Lignin model component
Guaiacol
Catalyst
Nickel–molybdenum/alumina
Hydrodeoxygenation
Deactivation by coking

ABSTRACT

Lignin is an aromatics' natural source that can be converted into separate high value chemical compounds. Due to the highly-functionalised network structure of phenols, the mechanisms, activity and selectivity of the acid-supported transition metal rate catalyst ($NiMo/Al_2O_3$) for the hydrogenation, hydrodeoxygenation (HDO) and defunctionalisation of (*l*) phase model components (eugenol, guaiacol and 4-propylguaiacol) were investigated in this integrated experimental, characterisation and modelling study. Commercially available $NiMo/Al_2O_3$ intermediates exhibited strongly acidic properties that did little to promote the complete bond saturation of the allyl-benzenes to alkyl-benzenes, thermodynamically-favoured higher molecular weight compositions (*e.g.* dimers) formed instead, and deactivation followed. The condensation elementary steps for an independent system constituent were proposed, which is important for understanding, designing and optimizing an efficient valorisation industrial processes engineering. Interestingly, the stabilising steric hindrances of different defined representatives affected product functionality distribution, reactivity and stability. HDO promoted demethoxylation (reaction), while methoxy-phenols were more favourably de-methylated. In addition, $NiMo/Al_2O_3$ formulation was analysed to obtain the quantified surface, structural and morphological changes by $NH_3$ activation temperature-programmed desorption (TPD), energy dispersive X-ray spectroscopy (EDS) mapping, Fourier transform infrared spectroscopy–attenuated total reflection (FTIR–ATR), nanometre computed tomography (nano-CT) and physi-sorption. Adsorbed carbonaceous species reduced its physicochemical interface, decreased by acidity.

## 1. Introduction

The petroleum-based chemicals and fuels are considered one of the most efficiently produced components in terms of energy efficiency. The exploitation of petroleum-based oil and lack of waste management combined with environmentally taxing production caused several environmental issues related to climate change and even the extinction of species (Chu and Karr, 2017). Therefore, sustainable and greener production of fuels, polymers (*e.g.* formaldehyde or epoxy resins), and chemicals made from renewable and bio-based material will play an essential role in the future (Mikulec et al., 2010; Ramirez and Rainey, 2019). Lignocellulosic (LC) biomass offers many exploitable constituents when we shift from petroleum-based compounds. The latter have attracted many researchers' attention in the last two decades. Lignin, a constituent of LC biomass, present in significant quantities, is the only aromatic biopolymer with a promising, highly functionalised, structure. The latter is outstandingly suitable for conversion to biofuels, aromatic building blocks in organic synthesis or precursors to fine chemicals (Gillet et al., 2017; Ročnik et al., 2022). However, its structure is neither trivial nor suitable for all bio-based products. The high oxygen content

* Corresponding author. Department of Catalysis and Chemical Reaction Engineering, National Institute of Chemistry, Hajdrihova 19, 1000, Ljubljana, Slovenia.
** Corresponding author.
*E-mail addresses:* edita.jasiukaityte@ki.si (E. Jasiukaitytė-Grojzdek), miha.grilc@ki.si (M. Grilc).

https://doi.org/10.1016/j.jclepro.2023.137701
Received 24 January 2023; Received in revised form 14 April 2023; Accepted 2 June 2023
Available online 3 June 2023

in lignin reduces its potential as a feedstock for fuels with low heating value, increased corrosivity and poor stability. The latter two factors could cause critical damage to process equipment or engines (Zhang et al., 2021). Therefore, removing oxygen-containing functional groups and implementing the hydrodeoxygenation (HDO) process is essential before further use as biofuels (Zhang et al., 2021). Alternatively, lignin or lignin-derived phenolics can be converted into products with additionally adjusted hydroxyl (OH) groups or substitution of other functional groups to more reactive OH groups (*e.g.* 1,2-dihydroxybenzene, 4-propylbenzene-1,2-diol) (Luo et al., 2018; Shu et al., 2018).

Demeth(ox)ylation and HDO of lignin-derived phenolics has been extensively studied in order to understand reaction mechanisms and catalyst efficiency to correlate structure-related information to defunctionalisation of the lignin macromolecule. However, the high efficiency of lignin valorisation in producing lignin-derived units, is decreased by the formation of undesired recalcitrant products. The main condensation pathway of lignin-like and monomeric intermediates proceeds through the formation of reactive phenolic hydroxyl or benzyl radicals, thus involving the emergence of new carbon-carbon bonds by forming aldehyde or quinone methide intermediates (Huang et al., 2014; Shao et al., 2021). Abad-Fernandez et al. (Abad-Fernández et al., 2020) proposed that condensation preferentially (kinetically) proceeds through monomeric units than from components with a higher amount of phenolic rings. On the other hand, Forchheim et al. (2014) reported that the lignin oligomeric units are the main facilitators of condensation, which leads to recalcitrant products. Additionally, the unsaturated side-chain was found to be the most reactive part of the molecule, looking at the condensation between the side-chain carbons and aromatic rings. In addition, they found that the guaiacyl units are the main constituents of recalcitrant products (Huang et al., 2014).

A commercially available and inexpensive catalyst, is a sulphidated transition-metal based material ($MoS_2$) promoted by Ni on an alumina ($\gamma$-$Al_2O_3$) support, which has been widely used for HDO in nonpolar solvents (He and Wang, 2012). The vacancies, located on the edges of $MoS_2$ nanoclusters, exhibit Lewis acidity and form strong metal-support interactions with the $\gamma$-$Al_2O_3$. The latter is immensely useful due to its excellent crushing strengths and high surface area (Hočevar et al., 2017; Oregui-Bengoechea et al., 2017; Ouedraogo and Bhoi, 2020). The catalytic sites on the catalyst are NiS and $MoS_x$, with the most active sites being the edges and vacancies. The combination of the two active sites is much more active than each of them individually (22 and 4 times, respectively) (Kubicka, 2019; Wagenhofer et al., 2017). To be precise, the most active parts of the catalyst are the $MoS_x$ edges decorated with Ni atoms, thus the active phase $NiMoS_x$ as predicted in the model. Presumably, the function of $MoS_x$ is the efficient adsorption of the active components, while the function of Ni is the more efficient $H_2$ activation (Žula et al., 2022). The $NiMo/Al_2O_3$ catalyst with defective $MoO_x$ structures and Ni-Mo alloy sites successfully catalysed the dehydroxylation and demethoxylation in the HDO process of guaiacol to cyclohexane (Zhang et al., 2021). Joshi et al. (Joshi and Lawal, 2013a) executed HDO of 4-propylguaiacol with $NiMo/Al_2O_3$ and found that 4-propylphenol is predominantly formed. On the other hand, it was reported that the acidity of the $\gamma$-$Al_2O_3$ support promoted the formation of methylated components over the catalysts (Mora-Vergara et al., 2018). Adsorbed components (catalyst coking) could significantly lower the catalyst activity, limit the mass transport within the catalyst pores, and lower the overall accessibility of the active sites. In the catalytic conversion of lignin model components, several HDO mechanisms have been reported. To date, condensation is the main challenge in lignin valorisation.

Several publications have already included microkinetic modelling as part of the fundamental understanding and describing HDO reaction mechanisms for biomass-derived components (Bjelić et al., 2018b, 2019; Ciesielski et al., 2020; Grilc et al., 2014; Pu et al., 2020; Ranzi et al., 2017; Ročnik et al., 2022). Bjelić et al. (Bjelić et al., 2018b, 2019) studied HDO of eugenol over carbon-supported noble metal catalysts (Ru, Rh, Pt, Pd, etc.). In their work, they performed a full kinetic study and found that hydrogenation of the unsaturated chain was the dominant step, followed by the hydrogenation of aromatic rings. On the other hand, moderate hydrogenation was observed over catalysts that included metallic and acidic active sites (alumina-supported Ru, Rh, Pt, Pd, etc.) (Bjelić et al., 2020). Microkinetic models assumed the Langmuir-Hinshelwood type of kinetics by presuming non-competitive adsorption of the component and hydrogen as the rate determining step (Bjelić et al., 2018a; Hočevar et al., 2019). In recent years, modelling has become an indispensable tool that allows understanding of the reaction mechanism, the behaviour of the system, and explaining chemical transformation.

In this work, we carried out HDO of lignin guaiacyl-type components (guaiacol, 4-propylguaiacol and eugenol) with bi-functional and bi-metallic $NiMo/Al_2O_3$ catalyst to examine the reactivity of the methoxy group, hydroxyl group and unsaturated side-chain. We have shown that the utilized material can restrain the aromatic structure during HDO. We further aim to understand the mechanism of condensation of lignin monomeric units, which is necessary to inhibit coupling reactions. Finally, the influence of the reaction temperature and pressure on the product distribution over time was studied. The primary focus of this study was to determine the link between the condensation of guaiacyl-type components and the stabilisation of reactive radicals. Therefore, microkinetic modelling was used to obtain kinetic parameters describing the correlation between the reaction rate and the activation energy for condensation and/or hydrogenation of the unsaturated double bond in the lignin model component. The kinetic parameters provide information about the behaviour of the guaiacyl-type components and the selective reactivity of the catalyst.

## 2. Experimental section

### 2.1. Materials

The chemicals, external calibration standards, gases and solvents were used without further purification. In this study we used; dimethyl disulphide (DMDS; >99 wt%, Sigma Aldrich, St. Louis, MO, USA, reference number 471569), 2-methoxyphenol (guaiacol; >99 wt%, Sigma Aldrich, St. Louis, MO, USA, reference number W253200), 2-methoxy-4-propylphenol (4-propylguaiacol; >99 wt%, Sigma Aldrich, St. Louis, MO, USA, reference number W359807), eugenol (>99 wt%, Sigma Aldrich, St. Louis, MO, USA, reference number E51791), 4-propylphenol (>97 wt%, Sigma Aldrich, St. Louis, MO, USA, reference number W364908), phenol (>99 wt%, Sigma Aldrich, St. Louis, MO, USA, reference number 33517), 1,2-dihydroxybenzene (catechol; >99 wt%, Sigma Aldrich, St. Louis, MO, USA, reference number 135011), 4-propylbenzene-1,2-diol (>95 wt%, Abcr, Karlsruhe, Germany, reference number AB563213), dodecane (>99 wt%, Sigma Aldrich, St. Louis, MO, USA, reference number 297879), C7–C30 saturated alkanes (1000 μg/mL each component in hexane, Supelco®, the chromatography division of Sigma Aldrich, St. Louis, MO, USA, reference number 49451-U), 3-methoxybiphenyl (>99 wt%, Aldrich$^{CPR}$, Sigma Aldrich, St. Louis, MO, USA, reference number S696862), 2,2′-biphenol (>99 wt%, Sigma Aldrich, St. Louis, MO, USA, reference number 115819), 2-benzylphenol (>98 wt%, Sigma Aldrich, St. Louis, MO, USA, reference number 13761), 2-phenoxy-1-phenylethanol (>97 wt%, Fluorochem, Hadfield, Derbyshire, United Kingdom, reference number 511533), nitrogen (5.0, Messer, Bad Soden am Taunus, Germany), hydrogen (5.0, Messer, Bad Soden am Taunus, Germany), hexane (>99 wt%, Sigma Aldrich, St. Louis, MO, USA, reference number 139386), xylenes (>98.5 wt%, Sigma Aldrich, St. Louis, MO, USA, reference number 247642).

### 2.2. Hydrodeoxygenation process

HDO experiments were performed in a 300 mL stainless steel batch reactor (Parker Autoclave Engineers, USA) with a Rushton turbine

impeller for optimal stirring (Fig. S1). Table 1 includes the most relevant reactions for further discussion while Table S1 includes the set of the reaction conditions applied in this work for microkinetic modelling. The total mass of reaction components was 105 g, of which 93.5 wt% of xylene (solvent), 3.7 wt% of monomeric component (eugenol, 4-propylguaiacol or guaiacol), 0.8 wt% of $NiMo/Al_2O_3$ (21 wt% of the catalyst with respect to the mass of the monomeric component) and 2 wt% of dodecane as the internal standard (IS). The system was purged three times with nitrogen, before finally flushed and pressurised with hydrogen, to ensure the reductive atmosphere. The agitation rate was kept constant at 1000 rpm. The reaction mixture was heated from room temperature to the desired final temperature with a heating rate 5 °C $min^{-1}$. After reaching the temperature plateau, the reactions were continued for 240 min. The reaction was stopped by rapid cooling by immersing the reactor to an ice bath.

### 2.3. Catalyst activation and characterisation

Bifunctional nickel-molybdenum catalyst on γ-$Al_2O_3$ support was used, either crushed and sieved to a fraction of 40–100 μm or in pelletized form. Prior to the experiment, the catalyst was dried in a $N_2$-purged furnace at 200 °C and sulphidated in the reactor with 20 mL of n-hexane and DMDS as the suphidating agent. The sulphidation protocol has been described in our previous publication (Grilc and Likozar, 2017).

The $NiMo/Al_2O_3$ catalyst was already thoroughly characterised in our previous works (Grilc et al., 2014; Grilc and Likozar, 2017; Hočevar et al., 2017). However, the specific surface area ($S_{BET}$) was determined by the Braunauer-Emmett-Teller model using an ASAP 2000 for $N_2$-physisorption (Micrometrics, Norcross, GA, USA). Temperature programme desorption of ammonia ($NH_3$-TPD) was conducted on the catalyst before and after the HDO process (Run 1) by using the Micrometrics AutoChem II Chemisorption Analyser (Micrometrics, Norcross, GA, USA). We additionally performed pyridine diffuse reflectance infrared Fourier transform spectroscopy (DRIFTS) on the fresh and the used samples using the Pike DiffusIR module in the PerkinElmer Spectrum 100 spectrometer. The spectra collected are the average of 16 scans with a resolution of 4 $cm^{-1}$. We performed energy-dispersive E-Ray spectroscopy (EDS) for elemental mapping on the pelletized form of $NiMo/Al_2O_3$ catalyst using scanning electron microscopy (SUPRA 35 VP, Carl Zeiss, Jena, Germany). Furthermore, the total carbon content (TOC; Rosemount Analytical Dohrmann DC-190, Santa Clara, CA, USA), elemental analysis (CHNS; vario EL cube, Elementar, Langenselbold, Germany) and nano-computed tomography (nano-CT) measurements were performed at NIC, IJS and UM, respectively.

Nano-computed tomography was used to analyse the internal structure of the catalysts. Samples were scanned with the 3D X-ray microscope ZEISS Xradia 620 Versa (Carl Zeiss AG, Oberkochen, Germany). All measurements were performed with the 4x objective at 40 kV and 3 W with LE3 filter. Exposure time was set to 1.6 s and binning to 4, resulting in a voxel size of 6.08 μm. Images were reconstructed using ZEISS Xradia software and Dragonfly software (Version 2021.1, Object Research Systems (ORS) Inc, Montreal, Canada, 2020).

The X-ray diffraction (XRD) analyses were performed on the PANalytical X'Pert Pro instrument using CuKα1 radiation source between 10° and 80°. The thermogravimetric analysis coupled with infrared spectroscopy (TG-FTIR) was performed on the PerkinElmer Spectrum 3 FTIR equipped with the EGA 4000 module. All the analysis were performed in a flow of synthetic air (20 ml $min^{-1}$, 20 vol% $O_2$ in $N_2$), from 40 °C to 450 °C at 10 K $min^{-1}$. The temperature 450 °C was chosen to prevent potential molybdenum oxide sublimation.

**Table 1**
Reaction conditions for each run in a batch reactor, where xylene was used as the solvent, $H_2$ as the reducing agent and $NiMo/Al_2O_3$ as the catalyst.

| Run | Model compound | T[a] (°C) | P[b] (MPa) |
|---|---|---|---|
| 1 | Eugenol | 275 | 1 |
| 2 | Eugenol[c] | 275 | 1 |
| 3 | Guaiacol | 275 | 1 |
| 4 | 4-Propylguaiacol | 275 | 1 |
| 5 | Eugenol[d] | 275 | 1 |
| 6 | Guaiacol[d] | 275 | 1 |

[a] Reaction temperature.
[b] Initial pressure in the reactor.
[c] Catalyst recycled from Run 1.
[d] Catalyst used in pellet form.

### 2.4. GC-MS analysis

The liquid samples were collected in 10-min intervals for the first hour, 20-min intervals for the second hour and 30-min intervals for the third and fourth hours. They were filtrated and diluted (50-fold) in xylene and analysed offline by gas chromatograph coupled with mass spectrometry (Shimadzu, Kyoto, Japan), equipped with a 60 m × 0.25 mm × 0.25 μm capillary column ZB-5MS (Phenomenex, Torrance, CA, USA) and a flame ionization detector (FID). The quantification of the identified monomeric products in the samples was performed based on the external 5-point calibration with standards purchased from Sigma-Aldrich. The concentration of a few more complex (dimeric and trimeric) products had to be determined by estimation based on the eugenol calibration curve and considered molar mass of complex product. For product identification, we used the retention indexes (RI) and the NIST 14 and FFNSC 2 libraries. The C7–C30 saturated alkane GC-MS standard was used to estimate the approximate RI of more complex products. Kováts RI were calculated by numerical interpolation by Equation (1) (Guardino et al., 1976),

$$RI = 100 \times \left( n \div \frac{\log t_x - \log t_n}{\log t_{n+1} - \log t_n} \right) \quad (1)$$

where $t_x$ is the retention time of the unknown component, $t_n$ and $t_{n+1}$ are the retention times of the saturated alkane standard ($t_n < t_x < t_{n+1}$) and n is the carbon number of the first saturated alkane used.

## 3. Microkinetic modelling

Hydrodeoxygenation of oxygen-containing lignin model compounds over $NiMo/Al_2O_3$ catalyst with hydrogen atmosphere took place in a three-phase system (reactor). The model is based on the model compounds pathway network and molar balances of each component influenced by the mass transfer between gaseous and bulk liquid (solvent) phase, and all components from the solvent phase to the catalyst surface, rates of adsorption, desorption and reactions on the catalyst active sites. We proposed a reaction mechanism (Fig. 1) by detected intermediates and products during liquid samples analysis. Each individual step was considered in the microkinetic model to determine contributions to the kinetic rates of oxygen-containing lignin model compounds. A detailed description of the model development was presented in our previous works (Bjelić et al., 2018b, 2019; Hočevar et al., 2017). In short, the key mass transfer rates and molar balances for compounds ($n$) are presented below.

Eq. (1), Eq. (2) and Eq. (3) were used to describe the mass transfer from the gas to liquid phase ($r_n^{GL}$), from the liquid phase to the catalyst surface ($r_n^{LS}$) and surface reaction rates ($c_n^s$), respectively. Indexes $g$, $l$, and $s$ refer to the gas, liquid and solid phase but components are not yet adsorbed on the solid-liquid interphase. The density and viscosity of xylene were calculated from the data available in the literature (Mulero and Cachadiña, 2014; Sebastian et al., 1981) and involved in calculations of transport phenomena, such as characteristic stirrer speed ($N^*$), Henry's constant ($He$), gas bubble diameter ($d_b$), gas-liquid transfer coefficient ($k_n^g$), gas-liquid interfacial surface ($A_g$), surface tension of liquid ($\sigma_l$), molar volume of a solvent ($V_D$), Schmidt number ($Sc$), diffusion

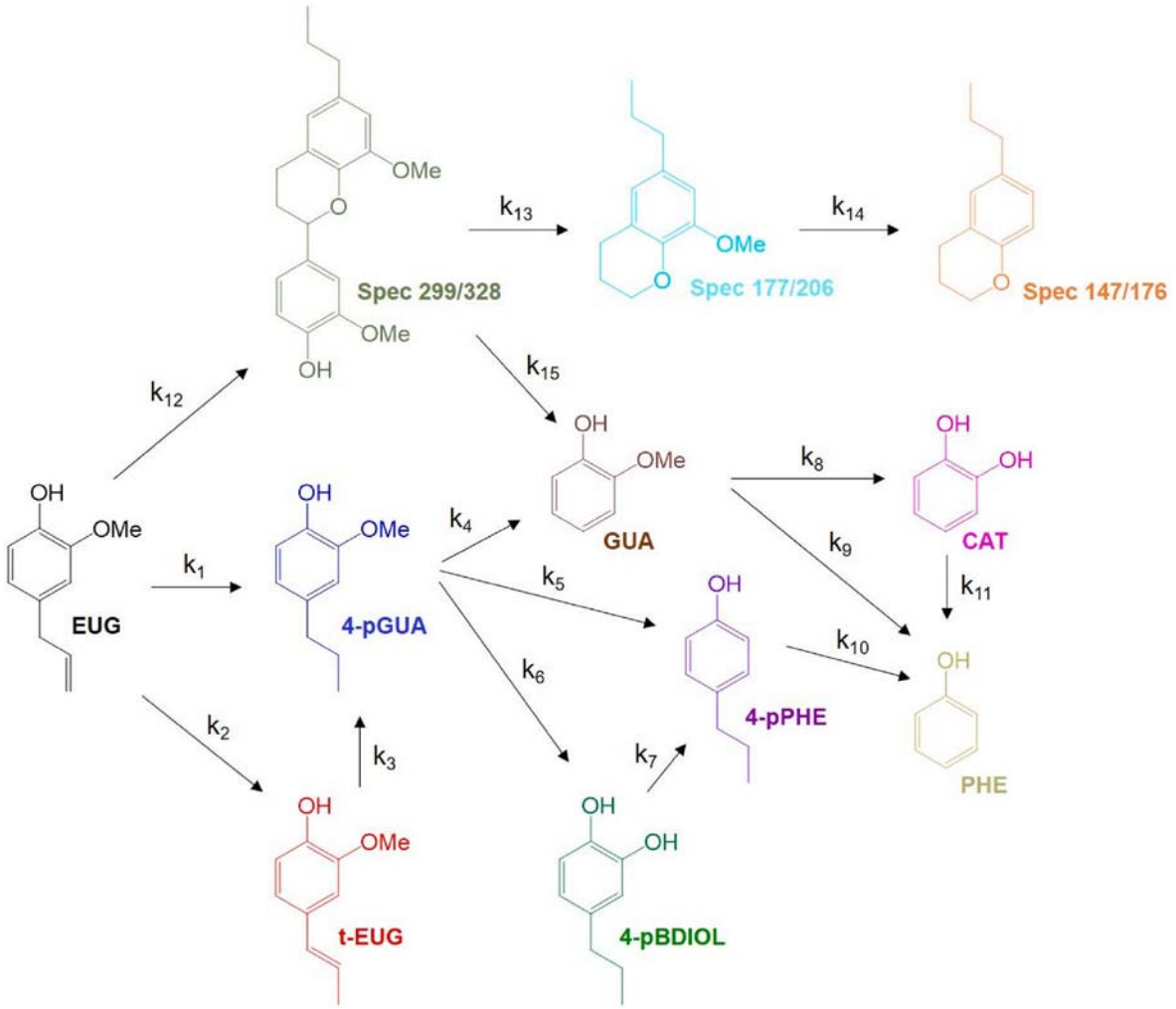


**Fig. 1.** Proposed reaction mechanism of eugenol HDO and coupling to repolymerised components over NiMo/$Al_2O_3$ catalyst.

coefficient ($D_{AB}$), liquid-solid mass transfer coefficient ($k_n^l$) and solid-liquid interfacial area ($A_s$). $p_n$ presents partial pressure of a component ($n$). Surface reaction rates were described as product of reaction constants ($k_n$) and surface coverages of reacting components ($c_n^s$). Further nomenclature, units, equations and correlations are the same as in our previous published works (Bjelić et al., 2020, 2019, 2018b, 2018a; Hočevar et al., 2017).

$$r_n^{GL} = k_n^g \times A_g \times \left(\frac{p_n}{He} - c_n^l\right) \quad (1)$$

$$r_n^{SL} = k_n^l \times A_s \times \left(c_n^l - c_n^s\right) \quad (2)$$

$$r_n = k_n \times c_n^s \quad (3)$$

The modelled values of the detected components were calculated by solving a set of differential equations describing the molar balances of all components. Molar balances for all reactants, intermediates and final products in the liquid phase, the liquid-solid interface and the catalyst surface, were considered. The process conditions (initial reactant concentration, mass of the catalyst, actual temperature and pressure, stirring rate and reaction time), the catalyst's characteristics (*e.g.*, specific surface area, the concentration of active sites) and reactor geometry were also involved in the model development.

The parameters modelled in this study were transport parameters $k_{ads}$ and $k_{des}$ (Table S2), $k_n$ and $Ea_n$, surface reaction rate constants and their corresponding activation energies, respectively. Our previous studies (Bjelić et al., 2018b, 2019) reported that the absence of external and internal mass transfer limitations is assured by agitation rate from 100 to 1000 rpm for catalyst particles in size of 50 μm. Moreover, the heat transfer effects were deemed to provide a negligible temperature gradient within the studied environment at a heating rate lower than 7.5 °C $min^{-1}$. Therefore, we applied a low heating rate of 5 °C $min^{-1}$ to improve heat transfer. Additionally, the solvent also serves as a heat buffer in case of eventual reaction enthalpy effects. In this study absence of mass and heat transfer limitations has been assured by intense mixing and a low heating rate.

The recycled catalyst run was fitted with change factors ($n$) in the form of Eq. (4), which shows the change in activity for each reaction except those following the suppressed reaction, since these could not be accurately described.

$$r_n = n \times k_n \times c_n^s \quad (4)$$

The model was coded using Matlab R2022a software. Kinetic rates and adsorption constants were calculated by the least squares minimization method using the combination of Nedler-Mead and Levenberg-Marquardt algorithms. The minimization equation is presented as Eq. (5) and is the sum of all squares of the differences between the experimental and model concentrations under the same experimental conditions simultaneously for all the experiments (EXP), samples collected (SAM) and components (COMP) followed. In the equation, $C$ represents the concentration of a compound, *exp* represents the experimentally obtained value, while *mod* represents the numerically obtained value, $i$

represents the time of the sample, while *j* represents the experiment.

$$f(k_n, Ea_n) = \sum_{j=1}^{EXP} \sum_{i=1}^{SAM} \sum_{C=1}^{COMP} \left( C_{j,i}^{exp} - C_{j,i}^{mod} \right)^2 \quad (5)$$

The differential equations were solved using the implicit Runge-Kutta formula with a trapezoidal rule step in the first stage and a backward differentiation formula of order two in the second stage, which was implemented as a Matlab ode23tb function.

## 4. Results

### 4.1. Hydrodeoxygenation results

GC-MS analysis of the liquid samples during eugenol (EUG) HDO over NiMo/$Al_2O_3$ has shown transeugenol (t-EUG), 4-propylguaiacol (4-pGUA), 4-propylphenol (4-pPHE) and guaiacol (GUA) to be the most dominant monomeric products while in lower concentration were 4-propyl-1,2-benzenediol (4-pBDIOL), catechol (CAT) and phenol (PHE). Among detected monomeric intermediates and products, the potential recalcitrant products (dimers or trimers) were formed (Fig. 2A and B). In the GC-MS spectrum, three recalcitrant products were detected with mass spectral fragmentation pattern of 147/176 (Mass Spec 147/176), 177/206 (Mass Spec 177/206) and 299/328 (Mass Spec 2997328) as shown in Fig. 3. Their structural composition (Fig. 3) has been proposed by interconnecting the results of mass spectrometry, retention times of C7–C30 saturated alkane standard (Table S3) and retention indexes of external dimeric calibration standards (Table 2). The external dimeric standards (3-methoxybiphenyl, 2,2′-biphenol, 2-benzylphenol and 2-phenoxy-1-phenylethanol) structurally have 12 to 14 carbon atoms, while comparison with C7–C30 standard pointed towards 16 to 18 carbon atoms in their structures. As C7–C30 standard is composed of linear saturated alkanes, the shift to a higher amount of carbon atoms measured of external dimeric standards (aromatic structure) is acceptable. However, we found that during the eugenol HDO recalcitrant products with mass spectral fragment of Mass Spec 147/176, Mass Spec 177/206 and Mass Spec 299/328 were formed with representative 15, 16 and 26 carbon atoms, respectively. Similarly, the number of carbon atoms in the proposed structure of unknown components (Fig. 3) is lower than the number of atoms estimated from the C7-C30 standard, probably due to the deviation between linear and aromatic structures.

The proposed structure and formation of dimeric or trimeric recalcitrant products are shown in Figs. 3 and 4, respectively. The coupling reaction could occur through electron transfer between the unsaturated side-chain of EUG and the reactive OH functional group. The new carbon-carbon bonds (condensation reaction) could be formed on the *ortho*- and *para*-positions by highly reactive phenolic hydroxyl groups involving quinone methide intermediates (Huang et al., 2014; Nakamura et al., 2007).

The mechanism of EUG HDO is presented in Fig. 1 with the relevant monomers and dimers. EUG simultaneously undergoes isomerization to t-EUG, and further conversion into p-GUA through the allyl group hydrogenation. Some EUG is involved in condensation to dimers by the proposed coupling mechanism depicted in Fig. 4 p-GUA is either demethylated to 4-pBDIOL, demethoxylated to 4-pPHE or dealkylated to GUA. Any 4-pBDIOL formed is gradually hydrodeoxygenated to 4-pPHE. Trace amounts of CAT and PHE have been detected during the EUG HDO as well. Moreover, we did not observe any components with the saturated aromatic rings (*e.g.*, cyclohexanes).

The product distribution of EUG hydrotreatment at the central conditions is displayed in Fig. 5A while Fig. S2 represents product distributions at the other conditions. Catalytic transformation of EUG was fast while the selectivity towards p-GUA was only 40 mol% within 60 min of reaction time. Formation of Spec 299/328 occurred in the first hour of the reaction during the ramp up to the final temperature and represented approximately 30 mol% of all detected components at 60 min. The

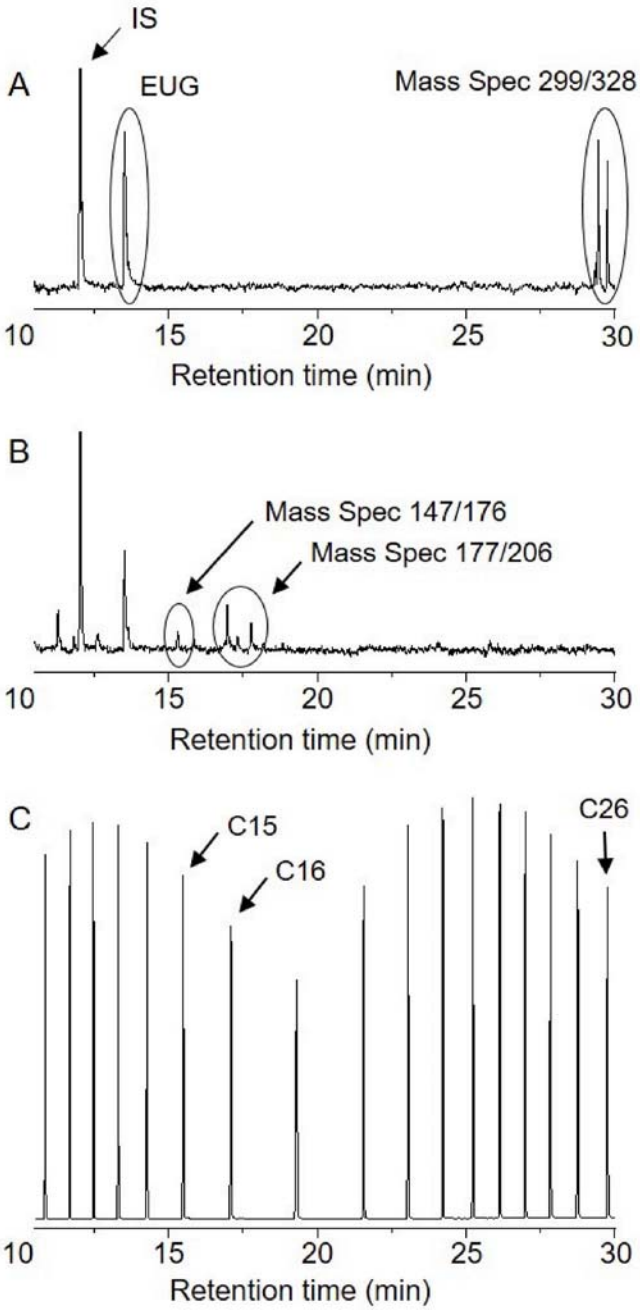


**Fig. 2.** Reconstructed GC-MS chromatograms. A: sampling time at 0 min for Run 1. B: sampling time at 100 min for Run 1. C: C7–C30 saturated alkane standard.

formed species contain a new carbon-carbon bond at the $C_5$-position in the guaiacyl unit. It was most likely formed by the binding of the tetrahydrofuran ring to the next guaiacyl unit via its alkyl group. Spec 177/206 and Spec 147/176 components were gradually formed through the cleavage of the C-C bond in the Spec 299/328 and demethoxylation (Fig. 3), respectively. The concentration of the components was inversely proportional and shifted, as bonding and cleavage occurred during the HDO process. Even though 4-pGUA was not fully converted (Fig. 5A), the main final products were 4-pPHE and 4-pBDIOL formed by demethoxylation and demethylation, respectively.

We performed recycle tests and the NiMo/$Al_2O_3$ catalyst was reused one time at the optimal conditions (275 °C, 1 MPa). The recycling of the catalyst notably affected the product distribution during the HDO

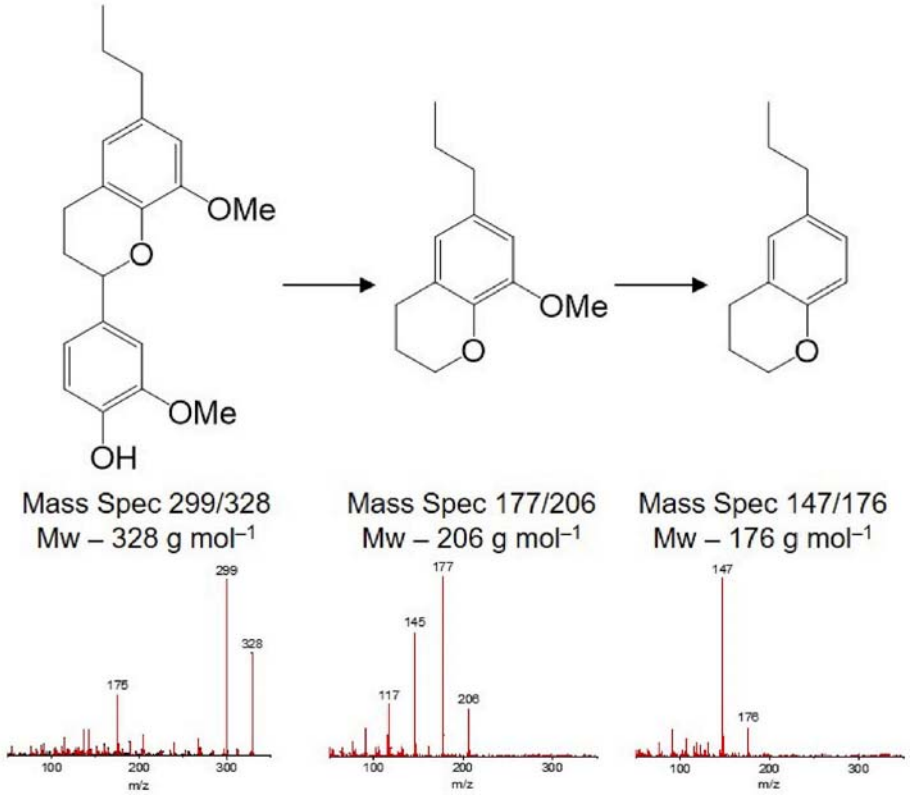


**Fig. 3.** Proposed structure of unknown components detected by GC-MS, mass spectral fragmentation pattern and cleavage mechanism.

**Table 2**
Retention indexes of the external calibration standards and detected products after eugenol HDO.

| Product name | Retention time (min) | Retention index |
|---|---|---|
| External calibration standards | | |
| 3-Methoxybiphenyl | 17.234 | 1605 |
| 2,2′-Biphenol | 17.709 | 1628 |
| 2-Benzylphenol | 18.067 | 1644 |
| 2-Phenoxy-1-phenylethanol | 21.714 | 1809 |
| Detected coupled products | | |
| Mass Spec 147/176 | 15.307 | 1483 |
| Mass Spec 177/206 | 17.426 | 1614 |
| Mass Spec 299/328 | 29.763 | 2598 |

process (Fig. 5B). The selectivity to p-GUA was increased significantly (up to 75 mol%) compared to the first use of the catalyst. Moreover, condensation of EUG to dimers decreased by 75 mol%. At the end of the reaction, the main product was 4-pBDIOL, while the conversion of 4-pGUA decreased by more than 70 mol%. Therefore, the NiMo/$Al_2O_3$ catalyst promoted demethylation over demethoxylation of 4-pGUA during the second run. When the recycled reaction was fitted with change factors (Table S5), the results confirmed the change in catalytic activity – the decrease in the amount of medium and strong acid sites was reflected in the decrease in the oligomerization constant ($k_{15}$), the lower amount of demethoxylation ($k_5$), dehydration ($k_7$), breaking of C-C bonds ($k_{10}$), and dimerization ($k_{12}$). Interestingly, isomerization was likely promoted by increasing the number of weak acid sites; however, the change may be overrepresented due to poor resolution between direct hydrogenation and isomerization.

We used GUA and 4-pGUA for mechanistic and coupling studies in

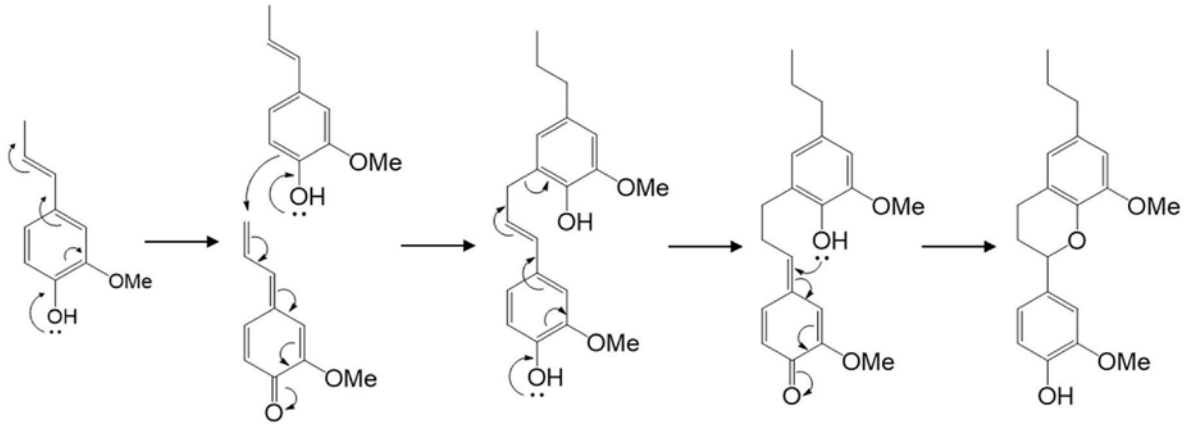


**Fig. 4.** Coupling mechanism through reactive OH group and unsaturated side-chain in eugenol. Adapted from reference (Nakamura et al., 2007).

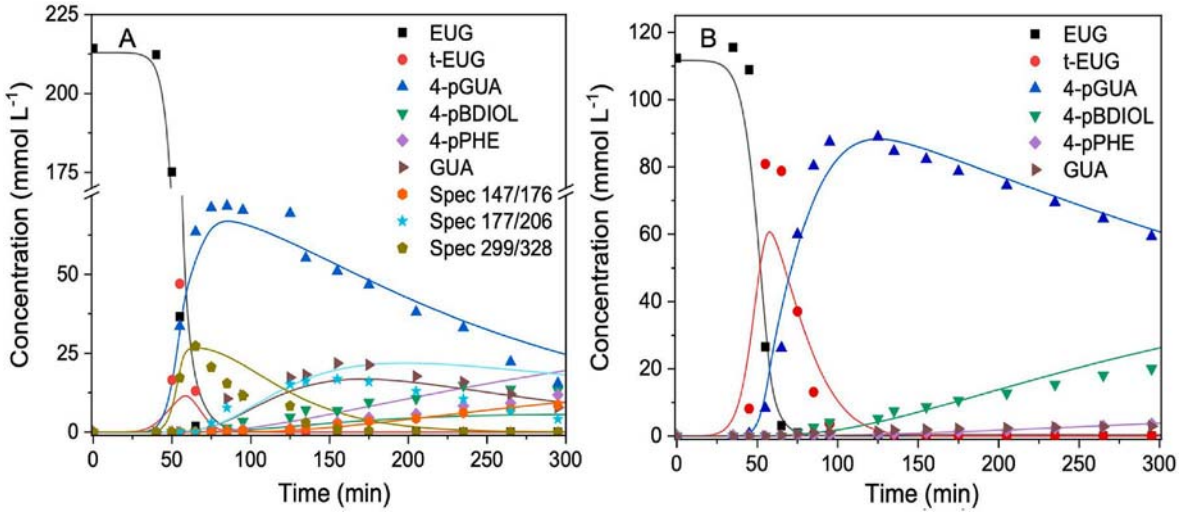


**Fig. 5.** HDO of EUG with (recycled-)NiMo/$Al_2O_3$ at 275 °C and 1 MPa $H_2$. A: EUG with NiMo/$Al_2O_3$ (Run 1), B: EUG with recycled NiMo/$Al_2O_3$ (Run 2).

order to determine the reactivity of the unsaturated side-chain of EUG at the optimal reaction conditions. GUA was mostly demethylated to CAT and somewhat HDO to PHE, while the conversion of GUA reached as much as 72 mol% (Fig. 6A). On the other hand, Zhang et al. (2021) prepared a NiMo/$Al_2O_3$ catalyst with hierarchical flower-like micro/-nanostructure to enhance the cooperative effect within the Ni-Mo alloy. The authors reported complete hydrogenation of GUA to cyclohexanes at 230 °C and 1 MPa initial hydrogen pressure.

The magnitudes of the bond strengths are influenced by the location and nature of the substituted functional groups (Parthasarathi et al., 2011). The oxygen-carbon bond $C_{(sp3)}$–OAr has a lower bond dissociation energy (BDE) (247 kJ $mol^{-1}$) than the $C_{(sp2)}$–OMe bond (356 kJ $mol^{-1}$) (Bui et al., 2011). Therefore, demethylation ($C_{(sp3)}$–OAr cleavage) is the primary reaction during the GUA HDO and a high yield of CAT is expected. Instead, 4-pGUA (Fig. 6B) was converted to 4-pPHE as the main product by demethoxylation while only a trace amount of 4-pBDIOL was detected. This is likely due to the allyl group, as it presents an additional steric hindrance during 4-pGUA HDO. Joshi et al. (Joshi and Lawal, 2013b) observed similar results with the dominant pathway being the formation of 4-pPHE, demethoxylation favoured over HDO or demethylation, during HDO of 4-pGUA.

### 4.2. Modelling results

The reaction rate constants (Table 3) and activation energies (Table S4) for HDO of EUG and its condensation were determined using kinetic model. From the calculated rate constants presented in Tables 3 and it is evident that the condensation is favoured over NiMo/$Al_2O_3$ compared to the hydrogenation of the EUG double bond. The condensation of the unsaturated bond by the OH group in EUG occurred at higher rates, $k_{10}$, compared to the hydrogenation of its double bond according to the estimated rate constants, $k_1$ and $k_3$. In fact, these heavier coupled products resulted in extreme mass loss in the first hour of HDO, which may be attributed to the highly acidic properties of the

**Table 3**
Reaction rate constants for the eugenol HDO at 275 °C.

| Reaction rate constants | $min^{-1}$ | Reaction rate constants | $min^{-1}$ |
|---|---|---|---|
| $k_1$ | 4.7 | $k_9$ | 0.6 |
| $k_2$ | 2.2 | $k_{10}$ | 0.9 |
| $k_3$ | 449 | $k_{11}$ | 0 |
| $k_4$ | 0 | $k_{12}$ | 15 |
| $k_5$ | 0.7 | $k_{13}$ | 12 |
| $k_6$ | 0.5 | $k_{14}$ | 1.1 |
| $k_7$ | 1 | $k_{olig}$ | 12.6 |
| $k_8$ | 0.9 | | |

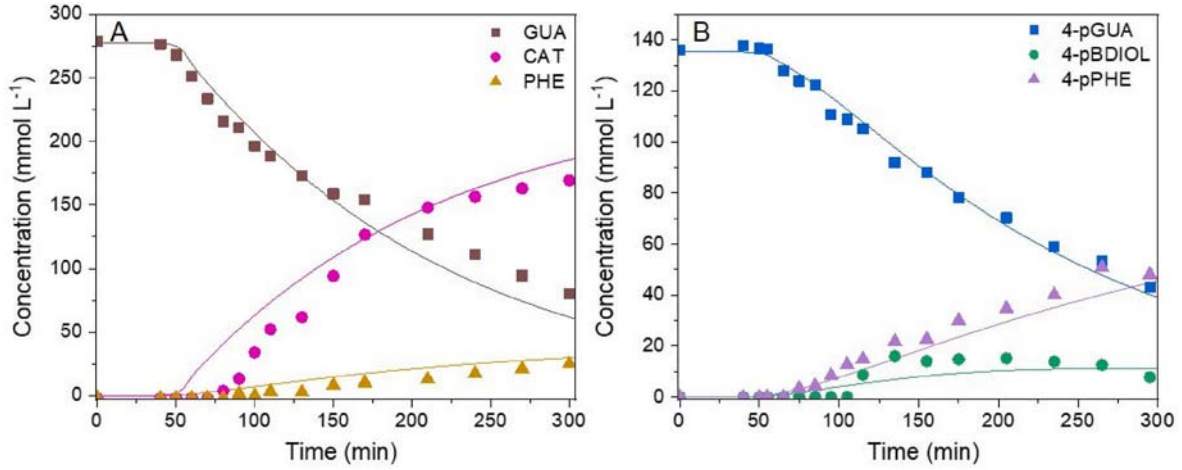


**Fig. 6.** HDO of GUA and 4-pGUA with NiMo/$Al_2O_3$ at 275 °C and 1 MPa $H_2$. A: GUA model component (Run 3), B: 4-pGUA model component (Run 4).

alumina support (Mora-Vergara et al., 2018; Nakamura et al., 2007). In contrast, the formation of condensed products was not reported for catalysts with noble metal particles on alumina support, where complete hydrogenation of the allyl group occurred (Bjelić et al., 2020). The decrease in mass balance was further neglected in the mathematical model to more accurately describe additional catalytic reactions. The high rate of 4-pGUA formation and the much lower rate of its conversion resulted in a high concentration of the intermediate over time. The demethoxylation of 4-pGUA to 4-pPHE is a faster reaction than the demethylation to 4-pBDIOL, whereas the kinetic model describes an inhibited formation of GUA. Moreover, 4-pBDIOL predominantly converted to 4-pPHE via HDO. The modelling results show that the demeth(ox)ylation reaction pathways have a significant contribution to the overall 4-pGUA HDO over $NiMo/Al_2O_3$, in contrast to the observations in the literature with much higher rate constants for its ring saturation over noble metal catalysts. Additionally, the removal of hydroxyl and methoxy functional groups from aromatic rings was reported to be more favourable than from the cyclohexane rings (Bjelić et al., 2018b, 2020).

The reaction rate constant of methyl group removal in GUA is reported to be 2-fold faster ($k_8$) than the removal of methoxy group to form PHE ($k_9$). Another way of PHE formation by removal of the hydroxyl group in CAT was not accounted ($k_{11}$). A different trend was observed for the model component 4-pGUA. Removal of the methoxy group in 4-pGUA was more favourable ($k_5$) than demethylation, with a 33% lower reaction rate constant ($k_6$). Moreover, the intermediate component 4-pBDIOL was hydrodeoxygenated to 4-pPHE at a higher rate ($k_7$) than the reaction constants $k_5$ and $k_6$. Thus, steric hindering ground were assumed to affect various preferential cleavage mechanisms of the functional groups arising from contact with the active sites of the catalyst and reactivity.

Oligomerization of heavy compounds was described with a $k_{olig}$ reaction whose product included mass balance loss during EUG conversion. The mechanism of this reaction most likely involves protonation over the catalyst acidic sites and reaction of the formed carbocation mainly with the aromatic ring which has nucleophilic nature (Sakhayi et al., 2021). The reaction product is the recalcitrant C-C bond and ultimately the formation of heavy oligomers, which are difficult to desorb from the surface. The reaction constant $k_{olig}$ was relatively high with a value of 12.6 $min^{-1}$, on the other hand, $Ea_{olig}$ was about 70 kJ $mol^{-1}$ higher than $Ea_1$ and 100 kJ $mol^{-1}$ higher than $Ea_2$ (Table S4), which means that the more complex lignin mixtures containing aliphatic double bonds should be treated at lower reaction temperatures over $NiMo/Al_2O_3$, which allows less formation of heavy oligomers.

### 4.3. Catalyst characterisation

Catalyst characterisation results are summarized in Table S6 and Table 4, and graphically supported by Figs. 7–11. Significant characterisation of the $NiMo/Al_2O_3$ catalyst was already published and described by our group (Grilc et al., 2014; Grilc and Likozar, 2017). In this manuscript we focused on the characterisation of the fresh, used and recycled $NiMo/Al_2O_3$ catalyst. With this, we correlated the catalyst properties with the condensation of the lignin model component.

**Table 4**
Integrated areas of the low and intermediate strength peaks in de-convolution of $NH_3$-TPD, and the total amount of desorbed ammonia up to approximately 400 °C.

| Peak temperature (°C) | Area (a.u.) | | |
|---|---|---|---|
| | Fresh | Run 1 | Run 2 |
| 63 | $4.33 \times 10^{-6}$ | $2.99 \times 10^{-6}$ | $5.22 \times 10^{-6}$ |
| 94 | $6.95 \times 10^{-6}$ | $5.30 \times 10^{-6}$ | $6.76 \times 10^{-6}$ |
| 150 | $8.88 \times 10^{-6}$ | $6.95 \times 10^{-6}$ | $6.17 \times 10^{-6}$ |
| 250 | $8.98 \times 10^{-6}$ | $2.89 \times 10^{-6}$ | $8.25 \times 10^{-7}$ |
| Amount of desorbed $NH_3$ | 1.19 mmol $g^{-1}$ | 0.83 mmol $g^{-1}$ | 0.89 mmol $g^{-1}$ |

To investigate the internal structure and composition of the $NiMo/Al_2O_3$ pellets before and after EUG (Run 5) and GUA (Run 6) HDO, EDS mapping and nano-CT were performed and compared. Before EDS was performed the catalysts were washed extensively with hexane. The elemental composition changes minimally between the fresh and used samples (Table S7), except for a notable increase in carbon (Fig. 7). The carbon content increased from 3.9 wt% for the fresh catalyst to 16.1 wt% after EUG HDO while only 8.1 wt% of carbon was detected on the catalyst surface after GUA HDO. These values support the theory that carbonaceous species irreversibly bind to the catalyst.

A result of a nano-CT image is a variation in grayscale intensities due to different X-ray absorption by different material features. Using the same parameters in the reconstruction process, a difference can be seen between the samples in both 2D slices as well as from 3D reconstructions. The colour spectrum of the 2D slice ranges from blue (lowest X-ray absorption) to red (highest X-ray absorption). As can be seen from the 2D slices, the number of specimens absorbing maximum X-rays (orange and red colour) is about the same for both samples. The difference can be seen in the structures with lower X-ray absorption, where there is a shift from green to blue for fresh and used catalyst (Fig. 8), respectively. The same observation was made in the 3D reconstruction images. The colour scale ranges from black (lowest X-ray absorption) to blue (highest X-ray absorption). Fig. 8D shows a very uniform structure throughout the used catalyst, while the inner part of the fresh catalyst appears to have a higher density (Fig. 8B). We assume that the irreversible binding of the carbonaceous species on the used catalysts reduces the X-ray absorption compared to the fresh catalyst, which can be seen as a shift from green to blue colour.

In Fig. 9, we present the results of ammonia temperature programmed desorption ($NH_3$-TPD). We performed the analysis on the fresh sample, a used sample without any after-treatment (Run 1), and the sample that was recycled one time (Run 2). The results presented in Fig. 9A have been normalized per mass of sample used for the analysis so that they can be compared directly. From the analyses, it is obvious, that after the HDO reaction a slight shift in acid sites occurs. The stronger acid sites, sites where $NH_3$ desorbs at higher temperatures, disappear, while the weaker acid sites increase slightly. We analysed the curves with the Fityk program (Table S8). We found that the ammonia desorption curves can be fitted with five separate peaks using the VoightA function. Focusing on the area up to 400 °C, since above this temperature water also desorbed from the catalyst, we found that there is a noticeable decrease in this intermediate acidity. The peak positioned at about 150 °C decreases by approximately 20 % after the first use, and a further 10 % after recycling. The difference is even more drastic in the peak positioned at about 250 °C. The corresponding acid sites decrease by almost 70 % after the first use, and additionally by over 70 % after recycling (Table 4). Overall, the acidity decreased by almost 30 %, from 1.19 mmol $NH_3$ $g^{-1}$ for the fresh catalyst to about 0.86 mmol $NH_3$ $g^{-1}$ for the used and recycled catalysts (Table 4).

We also performed DRIFT analysis combined with the pyridine adsorption, which is shown in Fig. 10. After pyridine adsorption, we observed the expected peaks, in line with the results reported in the literature (Deng et al., 2017; Hemmann et al., 2015; LEE and OYAMA, 2006; Loveless et al., 2008). Brønsted, as well as Lewis acid sites, cover the catalyst surfaces. We found a very good correlation with the results obtained by $NH_3$-TPD in that after use, the amount of acid sites drops. Surprisingly, no sites are preferentially covered, both Brønsted and Lewis sites are reduced.

To confirm that the source of the deactivation is EUG and other carbonaceous deposits covering the surface, we performed FTIR-ATR (attenuated total reflection) on fresh and used (and washed) catalysts (Fig. 11). It is obvious, by the peaks at 1750–1000 $cm^{-1}$, that the surface of the used material is covered by strongly bound carbonaceous species.

XRD analysis was performed to study the change in crystallinity of fresh and used catalyst. The XRD patterns showed negligible change in the crystalline phase of the catalysts (Fig. S3). To confirm the presence of

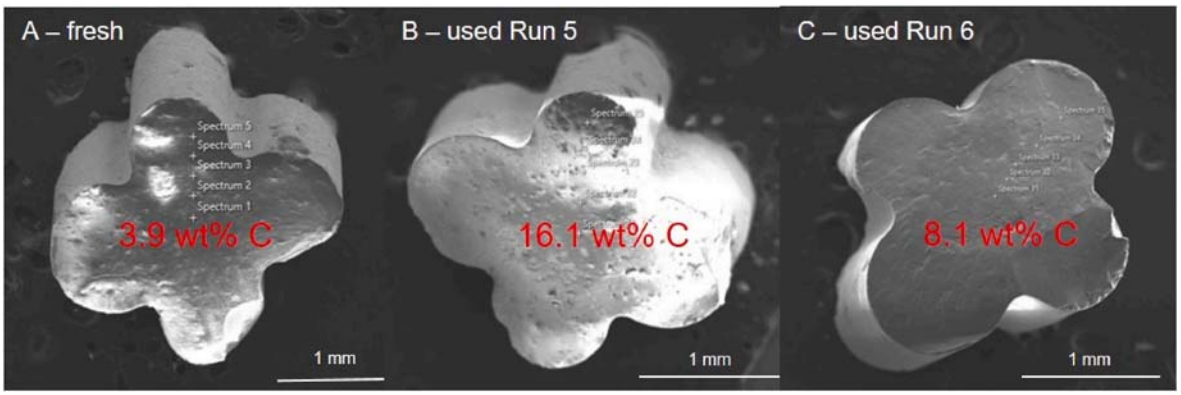


**Fig. 7.** SEM image and the measured carbon content of the $NiMo/Al_2O_3$ catalyst (A), $NiMo/Al_2O_3$ catalyst after EUG HDO (B) and $NiMo/Al_2O_3$ catalyst after GUA HDO (C).

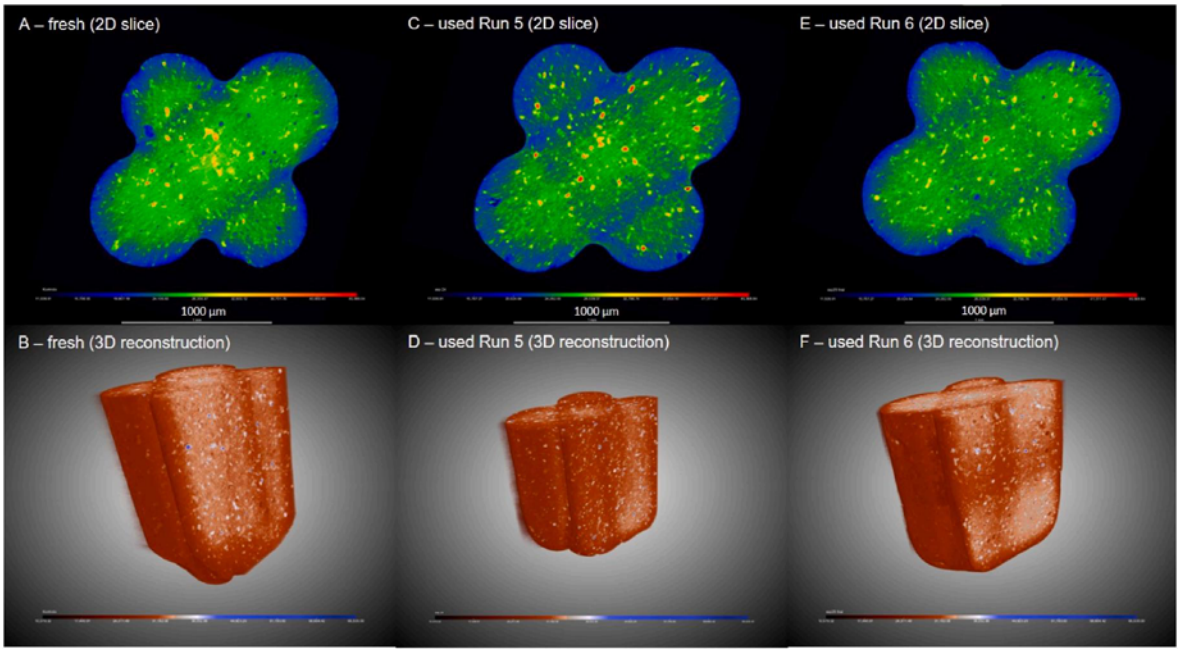


**Fig. 8.** Nano-CT images of fresh and used catalyst. A: fresh catalyst 2D slice, B: fresh catalyst 3D reconstruction, C: used (Run 5) catalyst 2D slice, D: used (Run 5) catalyst 3D reconstruction, E: used (Run 6) catalyst 2D slice and F: used (Run 6) catalyst 3D reconstruction.

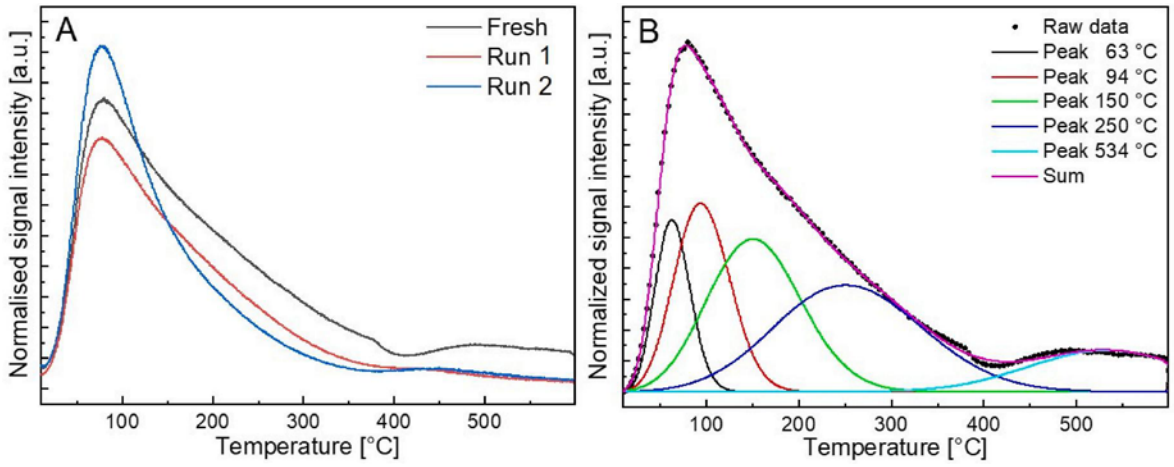


**Fig. 9.** Fragment 17 signal in $NH_3$-TPD intensity measured by MS, indicating ammonia desorption. Comparison of ammonia desorption between the fresh, the used, and the recycled samples (A). The deconvolution of the ammonia desorption from the fresh sample is shown in B.

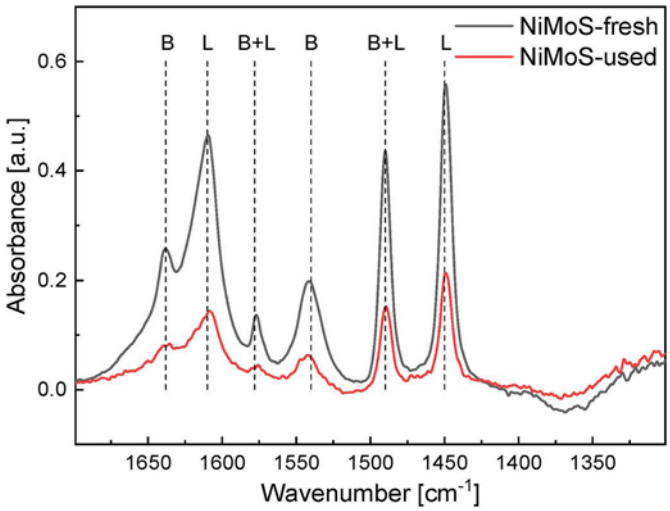


**Fig. 10.** DRIFT results of the fresh and used catalysts after pyridine adsorption.

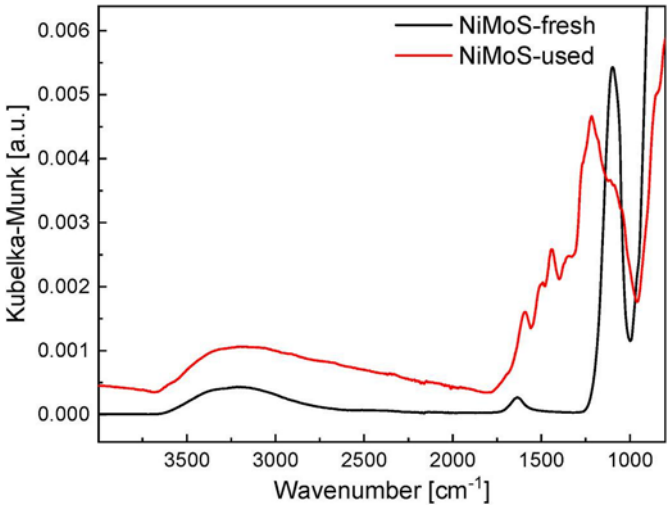


**Fig. 11.** FTIR-ATR results of the fresh and recycled (and washed) catalyst.

carbonaceous species populating the surface of the prepared catalysts we performed a coupled TG-FTIR analysis on the fresh and the used (Run 1) samples (Fig. 12). We found that, in the fresh, unused sample, most of the mass that is removed can be attributed to water and sulphur (Fig. S4). The greater part of water is removed up to 150 °C indicating that it is only physisorbed water, from atmospheric vapour. Up to 250 °C the total mass removed represents 13.4 % of the total mass. The sulphur is removed in the form of sulphur dioxide indicated by a very strong peak at 1375 $cm^{-1}$. The bulk of sulphur is removed after 250 °C. The relative mass drop attributed to sulphur is 10.4 %. The temporal profile of peak 2361 $cm^{-1}$ associated with $CO_2$ shows a negligible release of $CO_2$ from the fresh catalyst (Fig. S5).

The used sample exhibited a slightly different TG-FTIR profile. In the beginning, in contrast to the fresh sample, minimal water evolution was observed. Sulphur removal is shifted to slightly lower temperatures. The relative mass drop before 280 °C is just over 10 %. A significant part of sulphur species is removed simultaneously with surface carbonaceous species, hinting at some interaction of the species. The total relative mass removed from the fresh sample up to 450 °C is 20.3 %.

## 5. Discussion

The reaction mechanism and structures of coupling and recalcitrant products have been proposed over NiMo/$Al_2O_3$ with acidic properties which highly affect the condensation of lignin model component – eugenol. Among monomeric components, guaiacyl units, which contain $C_\alpha = C_\beta$ unsaturated side-chain and phenolic OH groups, were found to be the most reactive toward condensation between the side-chain carbons and aromatic rings (Huang et al., 2014). Besides, guaiacyl units were found to be the main constituents of lignin solid residue formation (Yong and Matsumura, 2012). Importantly, we detected no coupling products during the GUA and 4-pGUA HDO. Therefore, the unsaturated side-chain still dictates the condensation of lignin model components through reactive OH groups. However, the acidity of the alumina support enhances the formation of undesired or methyl-substituted components. The methyl group may stay adsorbed on the support surface enabling reactions with the aromatic rings of adsorbed components, such as CAT or PHE etc., by electrophilic substitution (Bui et al., 2011; Mora-Vergara et al., 2018). Mora-Vergara et al. (2018) reported that modification of acid-base properties of the potassium modified alumina support promoted complete demeth(ox)ylation of GUA and inhibited the formation of the undesired components.

On the other hand, NiMo/$Al_2O_3$ catalyst is beneficial for maintaining aromaticity (unsaturated aromatic rings). The potential reasons might be the stability of the aromatic ring in the presence of three substituents and transition metal active sites, the hindering effect of substituted functional groups on the aromatic ring, the acidity of the support (Mora-Vergara et al., 2018). Finally, the system exhibited low hydrogen availability since only an external hydrogen source was used in combination with a non-hydrogen donor solvent (Shafaghat et al., 2015).

In terms of the mechanism, reaction rates and other parameter

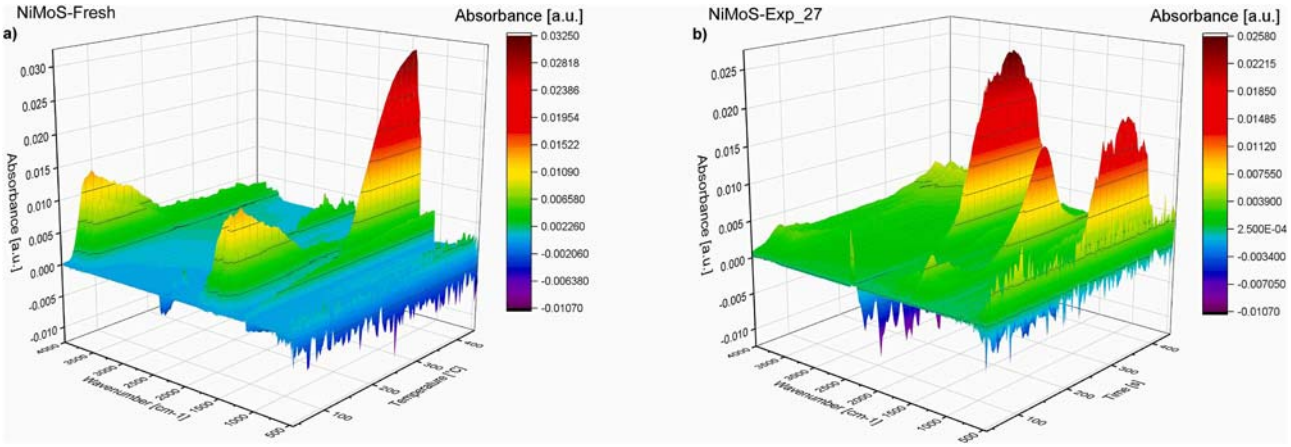


**Fig. 12.** Time-resolved data for the fresh and the used catalyst, showing the FTIR spectra of the evolved gasses during TG measurement.

examined in this study, we supported our results with comprehensive catalyst characterisation. $NiMo/Al_2O_3$ properties led to inefficient selectivity of the HDO process, and condensed components with higher molecular weight were formed and irreversibly bind to its surface. EDS mapping and the carbon content increased from 3.9 wt% for the fresh catalyst to 16.1 wt% after EUG HDO. Additionally, nano-CT images indicate that the carbonaceous species were homogeneously distributed on the surface of the used pelletized catalysts by the reduced the X-ray absorption compared to the fresh catalyst. We believe EUG and other carbonaceous deposits covered the catalysts active and acid sites. This, in turn, noticeably shifts the selectivity of the catalysts after reuse, additionally proven by kinetic modelling and change factors for HDO process when recycled catalyst was used. The results coincide very well with the results observed by DRIFT, ATR-FTIR, and TG-FTIR, indicating that the source of deactivation is the surface bound carbonaceous species.

## 6. Conclusion

The lignin model components eugenol, 4-propylguaiacol and guaiacol were used to investigate the importance of coupling reactions such as oligomerization and steric hindrances for product distribution during hydrotreatment.

*Coupling reaction effects:* Eugenol was involved in the condensation reaction between the electron transfer in the allyl side-chain and the reactive OH functional group by forming the quinone methide intermediate, while the condensation of 4-propylguaiacol and guaiacol was not detected. A catalyst with transition metal particles on an alumina support ($NiMo/Al_2O_3$) was tested for the HDO, whose acidic properties affected the process efficiency and selectivity. In comparison to the initial trials with the fresh catalyst, the reused catalyst revealed 75 mol% higher selectivity towards 4-propylguaiacol, while the formation of the undesired condensation products was reduced by 75 mol% when eugenol was used as lignin model component. However, due to the highly acidic sites on the catalyst surface and the HDO process, the catalyst properties changed after the process mainly because the carbonaceous species were irreversibly bound to the surface. Detailed characterization of the catalyst showed that eugenol was a possible adsorbed component.

*Steric hindrance effect:* Structural differences of the products suggest that similar lignin model components are defunctionalized via different mechanisms, specifically, demethoxylation and demethylation were more favourable for 4-propylguaiacol and guaiacol, respectively.

Finally, it should be pointed out that to significantly increase the efficiency of the lignin depolymerization it is important to examine various catalysts and not only different operating conditions. On the other hand, the use of the lignin model components is a limited approach for predicting lignin utilization because the reactivity of lignin bonds differs due to the steric hindrances and the local environment of the bonds, while the fundamental understanding of lignin condensation can only be studied using lignin model components because the lignin structure presents several challenges for determining functional groups and *in situ* monitoring of coupling reactions.

## CRediT authorship contribution statement

**Tina Ročnik Kozmelj:** Conceptualization, Methodology, Formal analysis, Investigation, Validation, Writing – original draft. **Matej Žula:** Methodology, Investigation, Writing – original draft. **Janvit Teržan:** Methodology, Formal analysis, Investigation, Writing – original draft. **Blaž Likozar:** Conceptualization, Visualization, Resources, Writing – review & editing. **Uroš Maver:** Supervision, Resources, Funding acquisition. **Laura Činč Ćurić:** Formal analysis, Investigation, Writing – original draft. **Edita Jasiukaitytė-Grojzdek:** Visualization, Supervision, Writing – review & editing. **Miha Grilc:** Resources, Supervision, Funding acquisition, Writing – review & editing.

## Declaration of competing interest

The authors declare that they have no known competing financial interests or personal relationships that could have appeared to influence the work reported in this paper.

## Data availability

Data will be made available on request.

## Acknowledgement

The authors acknowledge the financial support for this study received from the Slovenian Research Agency (grant numbers: J2–2492, J7–4492, P2–0152 and P3–0036).

## Appendix A. Supplementary data

Supplementary data to this article can be found online at https://doi.org/10.1016/j.jclepro.2023.137701.

## References

Abad-Fernández, N., Pérez, E., Martín, Á., Cocero, M.J., 2020. Kraft lignin depolymerisation in sub- and supercritical water using ultrafast continuous reactors. Optimization and reaction kinetics. J. Supercrit. Fluids 165. https://doi.org/10.1016/j.supflu.2020.104940.

Bjelić, A., Grilc, M., Gyergyek, S., Kocjan, A., Makovec, D., Likozar, B., 2018a. Catalytic hydrogenation, hydrodeoxygenation, and hydrocracking processes of a lignin monomer model compound eugenol over magnetic Ru/C–Fe2O3 and mechanistic reaction microkinetics. Catalysts 8. https://doi.org/10.3390/catal8100425.

Bjelić, A., Grilc, M., Huš, M., Likozar, B., 2019. Hydrogenation and hydrodeoxygenation of aromatic lignin monomers over Cu/C, Ni/C, Pd/C, Pt/C, Rh/C and Ru/C catalysts: mechanisms, reaction micro-kinetic modelling and quantitative structure-activity relationships. Chem. Eng. J. 359, 305–320. https://doi.org/10.1016/j.cej.2018.11.107.

Bjelić, A., Grilc, M., Likozar, B., 2020. Bifunctional metallic-acidic mechanisms of hydrodeoxygenation of eugenol as lignin model compound over supported Cu, Ni, Pd, Pt, Rh and Ru catalyst materials. Chem. Eng. J. 394, 124914 https://doi.org/10.1016/j.cej.2020.124914.

Bjelić, A., Grilc, M., Likozar, B., 2018b. Catalytic hydrogenation and hydrodeoxygenation of lignin-derived model compound eugenol over Ru/C: intrinsic microkinetics and transport phenomena. Chem. Eng. J. 333, 240–259. https://doi.org/10.1016/j.cej.2017.09.135.

Bui, V.N., Laurenti, D., Delichère, P., Geantet, C., 2011. Hydrodeoxygenation of guaiacol. Part II: support effect for CoMoS catalysts on HDO activity and selectivity. Appl. Catal. B Environ. 101, 246–255. https://doi.org/10.1016/j.apcatb.2010.10.031.

Chu, E.W., Karr, J.R., 2017. Environmental impact: concept, consequences, measurement. In: Reference Module in Life Sciences. Elsevier. https://doi.org/10.1016/B978-0-12-809633-8.02380-3.

Ciesielski, P.N., Pecha, M.B., Lattanzi, A.M., Bharadwaj, V.S., Crowley, Meagan F., Bu, L., Vermaas, J.V., Steirer, K.X., Crowley, Michael F., 2020. Advances in multiscale modeling of lignocellulosic biomass. ACS Sustain. Chem. Eng. 8, 3512–3531. https://doi.org/10.1021/acssuschemeng.9b07415.

Deng, J., Liu, Jixing, Song, W., Zhao, Z., Zhao, L., Zheng, H., Lee, A.C., Chen, Y., Liu, Jian, 2017. Selective catalytic reduction of NO with NH 3 over Mo–Fe/beta catalysts: the effect of Mo loading amounts. RSC Adv. 7, 7130–7139. https://doi.org/10.1039/C6RA27126J.

Forchheim, D., Hornung, U., Kruse, A., Sutter, T., 2014. Kinetic modelling of hydrothermal lignin depolymerisation. Waste and Biomass Valorization 5, 985–994. https://doi.org/10.1007/s12649-014-9307-6.

Gillet, S., Aguedo, M., Petitjean, L., Morais, A.R.C., Da Costa Lopes, A.M., Łukasik, R.M., Anastas, P.T., 2017. Lignin transformations for high value applications: towards targeted modifications using green chemistry. Green Chem. 19, 4200–4233. https://doi.org/10.1039/c7gc01479a.

Grilc, M., Likozar, B., 2017. Levulinic acid hydrodeoxygenation, decarboxylation and oligmerization over NiMo/Al2O3 catalyst to bio-based value-added chemicals: modelling of mass transfer, thermodynamics and micro-kinetics. Chem. Eng. J. 330, 383–397. https://doi.org/10.1016/j.cej.2017.07.145.

Grilc, M., Likozar, B., Levec, J., 2014. Hydrodeoxygenation and hydrocracking of solvolysed lignocellulosic biomass by oxide, reduced and sulphide form of NiMo, Ni, Mo and Pd catalysts. Appl. Catal. B Environ. 150–151, 275–287. https://doi.org/10.1016/j.apcatb.2013.12.030.

Guardino, X., Albaigés, J., Firpo, G., Rodríguez-Viñals, R., Gassiot, M., 1976. Accuracy in the determination of the Kováts retention index. Mathematical dead time. J. Chromatogr. A. https://doi.org/10.1016/S0021-9673(00)81026-2.

He, Z., Wang, X., 2012. Hydrodeoxygenation of model compounds and catalytic systems for pyrolysis bio-oils upgrading. Catal. Sustain. Energy 1. https://doi.org/10.2478/cse-2012-0004.

Hemmann, F., Agirrezabal-Telleria, I., Jaeger, C., Kemnitz, E., 2015. Quantification of acidic sites of nanoscopic hydroxylated magnesium fluorides by FTIR and 15 N MAS NMR spectroscopy. RSC Adv. 5, 89659–89668. https://doi.org/10.1039/C5RA15116C.

Hočevar, B., Grilc, M., Huš, M., Likozar, B., 2019. Mechanism, ab initio calculations and microkinetics of straight-chain alcohol, ether, ester, aldehyde and carboxylic acid hydrodeoxygenation over Ni-Mo catalyst. Chem. Eng. J. 359, 1339–1351. https://doi.org/10.1016/j.cej.2018.11.045.

Hočevar, B., Grilc, M., Huš, M., Likozar, B., 2017. Mechanism, ab initio calculations and microkinetics of hydrogenation, hydrodeoxygenation, double bond migration and cis–trans isomerisation during hydrotreatment of C6 secondary alcohol species and ketones. Appl. Catal. B Environ. 218, 147–162. https://doi.org/10.1016/j.apcatb.2017.06.046.

Huang, X., Korányi, T.I., Boot, M.D., Hensen, E.J.M., 2014. Catalytic depolymerization of lignin in supercritical ethanol. ChemSusChem 7, 2276–2288. https://doi.org/10.1002/cssc.201402094.

Joshi, N., Lawal, A., 2013a. Hydrodeoxygenation of 4-propylguaiacol (2-methoxy-4-propylphenol) in a microreactor: performance and kinetic studies. Ind. Eng. Chem. Res. 52, 4049–4058. https://doi.org/10.1021/ie400037y.

Joshi, N., Lawal, A., 2013b. Hydrodeoxygenation of 4-propylguaiacol (2-methoxy-4-propylphenol) in a microreactor: performance and kinetic studies. Ind. Eng. Chem. Res. 52, 4049–4058. https://doi.org/10.1021/ie400037y.

Kubicka, D., 2019. Upgrading of lipids to hydrocarbon fuels via (hydro)deoxygenation. Chem. Catal. Biomass Upgrad. 469–496. https://doi.org/10.1002/9783527814794.ch11.

Lee, Y., Oyama, S., 2006. Bifunctional nature of a SiO2-supported Ni2P catalyst for hydrotreating: EXAFS and FTIR studies. J. Catal. 239, 376–389. https://doi.org/10.1016/j.jcat.2005.12.029.

Loveless, B.T., Gyanani, A., Muggli, D.S., 2008. Discrepancy between TPD- and FTIR-based measurements of Brønsted and Lewis acidity for sulfated zirconia. Appl. Catal. B Environ. 84, 591–597. https://doi.org/10.1016/j.apcatb.2008.05.025.

Luo, G., Jiao, Y., Lv, X., Zhang, X., Gao, X., 2018. Green synthesis of dihydroxybenzene from phenol with hydrogen peroxide catalyzed by iron modified FSM-16. Res. Chem. Intermed. 44, 5377–5387. https://doi.org/10.1007/s11164-018-3428-7.

Mikulec, J., Cvengroš, J., Joríková, Ľ., Banič, M., Kleinová, A., 2010. Second generation diesel fuel from renewable sources. J. Clean. Prod. 18, 917–926. https://doi.org/10.1016/j.jclepro.2010.01.018.

Mora-Vergara, I.D., Hernández Moscoso, L., Gaigneaux, E.M., Giraldo, S.A., Baldovino-Medrano, V.G., 2018. Hydrodeoxygenation of guaiacol using NiMo and CoMo catalysts supported on alumina modified with potassium. Catal. Today 302, 125–135. https://doi.org/10.1016/j.cattod.2017.07.015.

Mulero, A., Cachadiña, I., 2014. Recommended correlations for the surface tension of several fluids included in the REFPROP program. J. Phys. Chem. Ref. Data 43. https://doi.org/10.1063/1.4878755.

Nakamura, T., Kawamoto, H., Saka, S., 2007. Condensation reactions of some lignin related compounds at relatively low pyrolysis temperature. J. Wood Chem. Technol. 27, 121–133. https://doi.org/10.1080/02773810701515143.

Oregui-Bengoechea, M., Gandarias, I., Miletić, N., Simonsen, S.F., Kronstad, A., Arias, P. L., Barth, T., 2017. Thermocatalytic conversion of lignin in an ethanol/formic acid medium with NiMo catalysts: role of the metal and acid sites. Appl. Catal. B Environ. 217, 353–364. https://doi.org/10.1016/j.apcatb.2017.06.004.

Ouedraogo, A.S., Bhoi, P.R., 2020. Recent progress of metals supported catalysts for hydrodeoxygenation of biomass derived pyrolysis oil. J. Clean. Prod. 253, 119957 https://doi.org/10.1016/j.jclepro.2020.119957.

Parthasarathi, R., Romero, R.A., Redondo, A., Gnanakaran, S., 2011. Theoretical study of the remarkably diverse linkages in lignin. J. Phys. Chem. Lett. 2, 2660–2666. https://doi.org/10.1021/jz201201q.

Pu, J., Laurenti, D., Geantet, C., Tayakout-Fayolle, M., Pitault, I., 2020. Kinetic modeling of lignin catalytic hydroconversion in a semi-batch reactor. Chem. Eng. J. 386, 122067 https://doi.org/10.1016/j.cej.2019.122067.

Ramirez, J.A., Rainey, T.J., 2019. Comparative techno-economic analysis of biofuel production through gasification, thermal liquefaction and pyrolysis of sugarcane bagasse. J. Clean. Prod. 229, 513–527. https://doi.org/10.1016/j.jclepro.2019.05.017.

Ranzi, E., Debiagi, P.E.A., Frassoldati, A., 2017. Mathematical modeling of fast biomass pyrolysis and bio-oil formation. Note I: kinetic mechanism of biomass pyrolysis. ACS Sustain. Chem. Eng. 5, 2867–2881. https://doi.org/10.1021/acssuschemeng.6b03096.

Ročnik, T., Likozar, B., Jasiukaitytė-Grojzdek, E., Grilc, M., 2022. Catalytic lignin valorisation by depolymerisation, hydrogenation, demethylation and hydrodeoxygenation: mechanism, chemical reaction kinetics and transport phenomena. Chem. Eng. J. 448, 137309 https://doi.org/10.1016/j.cej.2022.137309.

Sakhayi, A., Bakhtyari, A., Rahimpour, M.R., 2021. Cleaner production of liquid fuels and chemicals by synthesis-gas-assisted hydroprocessing of lignin compounds as biomass-derivates. J. Clean. Prod. 316, 128331 https://doi.org/10.1016/j.jclepro.2021.128331.

Sebastian, H.M., Lin, H.M., Chao, K.C., 1981. Correlation of solubility of hydrogen in hydrocarbon solvents. AIChE J. 27, 138–148. https://doi.org/10.1002/aic.690270120.

Shafaghat, H., Sirous Rezaei, P., Daud, W.M.A.W., 2015. Catalytic hydrogenation of phenol, cresol and guaiacol over physically mixed catalysts of Pd/C and zeolite solid acids. RSC Adv. 5, 33990–33998. https://doi.org/10.1039/c5ra00367a.

Shao, S., Hu, X., Dong, W., Li, X., Zhang, H., Xiao, R., Cai, Y., 2021. Integrated C–C coupling/hydrogenation of ketones derived from biomass pyrolysis for aviation fuel over Ni/Mg–Al–O/AC bifunctional catalysts. J. Clean. Prod. 282, 124331 https://doi.org/10.1016/j.jclepro.2020.124331.

Shu, R., Xu, Y., Ma, L., Zhang, Q., Wang, C., Chen, Y., 2018. Controllable production of guaiacols and phenols from lignin depolymerization using Pd/C catalyst cooperated with metal chloride. Chem. Eng. J. 338, 457–464. https://doi.org/10.1016/j.cej.2018.01.002.

Wagenhofer, M.F., Baráth, E., Gutiérrez, O.Y., Lercher, J.A., 2017. Carbon-carbon bond scission pathways in the deoxygenation of fatty acids on transition-metal sulfides. ACS Catal. 7, 1068–1076. https://doi.org/10.1021/acscatal.6b02753.

Yong, T.L.K., Matsumura, Y., 2012. Reaction kinetics of the lignin conversion in supercritical water. Ind. Eng. Chem. Res. 51, 11975–11988. https://doi.org/10.1021/ie300921d.

Zhang, Y., Fan, G., Yang, L., Zheng, L., Li, F., 2021. Cooperative effects between Ni-Mo alloy sites and defective structures over hierarchical Ni-Mo bimetallic catalysts enable the enhanced hydrodeoxygenation activity. ACS Sustain. Chem. Eng. 9, 11604–11615. https://doi.org/10.1021/acssuschemeng.1c04762.

Žula, M., Grilc, M., Likozar, B., 2022. Hydrocracking, hydrogenation and hydrodeoxygenation of fatty acids, esters and glycerides: mechanisms, kinetics and transport phenomena. Chem. Eng. J. 444 https://doi.org/10.1016/j.cej.2022.136564.